Surface Ocean Mixing Inferred from Different Multisatellite Altimetry Measurements

FRANCISCO J. BERON-VERA AND MARÍA J. OLASCOAGA

Rosenstiel School of Marine and Atmospheric Science, University of Miami, Miami, Florida

GUSTAVO J. GONI

National Oceanic and Atmospheric Administration Atlantic Oceanographic and Meteorological Laboratory, Miami, Florida

(Manuscript received 1 March 2010, in final form 31 May 2010)

ABSTRACT

Two sea surface height (SSH) anomaly fields distributed by Archiving, Validation, and Interpretation of Satellite Oceanographic (AVISO) Altimetry are evaluated in terms of the effects that they produce on mixing. One SSH anomaly field, tagged REF, is constructed using measurements made by two satellite altimeters; the other SSH anomaly field, tagged UPD, is constructed using measurements made by up to four satellite altimeters. Advection is supplied by surface geostrophic currents derived from the total SSH fields resulting from the addition of these SSH anomaly fields to a mean SSH field. Emphasis is placed on the extraction from the currents of Lagrangian coherent structures (LCSs), which, acting as skeletons for patterns formed by passively advected tracers, entirely control mixing. The diagnostic tool employed to detect LCSs is provided by the computation of finite-time Lyapunov exponents. It is found that currents inferred using UPD SSH anomalies support mixing with characteristics similar to those of mixing produced by currents inferred using REF SSH anomalies. This result mainly follows from the fact that, being more easily characterized as chaotic than turbulent, mixing as sustained by currents derived using UPD SSH anomalies is quite insensitive to spatiotemporal truncations of the advection field.

1. Introduction

The purpose of this study is to carry out an evaluation of two altimetry products distributed by the Archiving, Validation, and Interpretation of Satellite Oceanographic (AVISO) Altimetry data center with a focus on surface ocean mixing.[1] The AVISO products considered are sea surface height (SSH) anomaly fields that differ by the number of satellite altimeters that furnish the measurements employed in their construction. One SSH anomaly field, tagged REF, is constructed using measurements made by two satellite altimeters that occupied the same groundtracks throughout the whole record. The second SSH anomaly field, tagged UPD, is constructed using measurements made by a different number of satellites throughout the record, ranging from two to four. The total SSH fields resulting from adding these SSH anomaly fields to a mean SSH field are used to compute surface geostrophic currents, which provide advection for the Lagrangian calculations presented in this work. The surface geostrophic currents that use UPD SSH anomalies in their computation are referred to as UPD currents throughout this work and those that involve REF SSH anomalies as REF currents.

Various studies of the differences between SSH anomaly fields similar to those considered here have been reported. For instance, Pascual et al. (2006) reported larger SSH anomalies and enhanced eddy kinetic energies when measurements from four satellite altimeters are combined. Improved consistency was also noted by Pascual et al. between altimetric SSH measurements and tidal gauge data in coastal areas. In addition, Chelton et al. (2007) reported improved agreement between theoretical Rossby wave phase speeds and phase speeds of low-frequency SSH anomaly signals when UPD SSH anomalies are considered.

On the other hand, global (Beron-Vera et al. 2008; Waugh and Abraham 2008) and regional (Abraham and

[1] Throughout this work, mixing is understood as the nondiffusive rearrangement of parcels of fluid particles resulting from the successive stretching and folding exclusively produced by lateral advection.

Corresponding author address: F. J. Beron-Vera, RSMAS/AMP, University of Miami, 4600 Rickenbacker Cswy., Miami, FL 33149.
E-mail: fberon@rsmas.miami.edu.

DOI: 10.1175/2010JPO4458.1

Bowen 2002; d'Ovidio et al. 2008; Rossi et al. 2009; Waugh et al. 2006) Lagrangian calculations have provided support for the notion that mixing as sustained by UPD currents is largely heterogeneous, with the velocity field being largely spatially coherent and temporally regular on time scales over which fluid particle motion is mainly irregular. Consistent with this notion, Shuckburgh et al. (2009) reported very small sensitivity of effective diffusivity calculations to spatial smoothing of UPD currents in a study carried out in the Pacific sector of the Southern Ocean. These results suggest that the differences between UPD and REF currents should have a small effect on mixing, which we seek to investigate.

With the above goal in mind we place particular focus on the detection of Lagrangian coherent structures (LCSs). As defined in Haller and Yuan (2000), LCSs constitute distinguished invariant manifolds in the augmented (by the time coordinate) phase space of a nonautonomous dynamical system. By ''nonautonomous dynamical system'' it is meant a set of first-order ordinary differential equations with explicit dependence on time, whereas by ''invariant manifold'' it is meant a surface composed of solution curves or trajectories of the system. Fluid particle trajectories, as produced by a two-dimensional velocity field such as the UPD and REF velocity fields, obey a system of the aforementioned type. As viewed from the corresponding phase space (i.e., the physical two-dimensional space) LCSs are (time evolving) material fluid curves that act as skeletons for patterns formed by passively advected tracers. More specifically, attracting (repelling) LCSs are material fluid curves that attract (repel) neighboring fluid particles at the highest rate over a finite interval of time. As such, attracting LCSs provide a theoretical foundation for the filamentary distributions commonly attained by passive tracers. Repelling LCSs, in turn, supply a theoretical basis for sustaining the maximal local stretching fluid regions. LCSs cannot be revealed visually from the inspection of velocity field snapshots. Thus, an appropriate technique is required to detect them. Here we consider finite-time Lyapunov exponents (FTLEs), which supply a quite practical and robust LCS detection technique (Haller 2001a,b, 2002; Shadden et al. 2005); other diagnostic tools exist that also reveal LCSs (e.g., Boffetta et al. 2001; Haller 2001b; Joseph and Legras 2002). The forward (backward) FTLE characterizes the amount of forward (backward) time stretching about fluid particle trajectories. Ridges of forward (backward) FTLE field, defined as curves about which the forward (backward) FTLE falls off fastest, correspond to regions of maximal repulsion (attraction) and, thus, generally qualify as LCSs. The FTLE technique has been applied extensively in recent years (e.g., Beron-Vera and Olascoaga 2009; Beron-Vera et al. 2008, 2010; Franco et al. 2007; Green et al. 2007; Lekien and Coulliette 2007; Lekien et al. 2007; Mathur et al. 2007; Olascoaga et al. 2006, 2008; Padberg et al. 2007; Reniers et al. 2010; Rypina et al. 2009; Salman et al. 2007; Shadden et al. 2006, 2009). A review on the use of the FTLE technique in LCS detection is given in Peacock and Dabiri (2010).

A main conclusion of the evaluation presented here is that the differences between the UPD and REF SSH anomaly fields distributed by AVISO have a small impact on the statistics of surface ocean mixing as sustained by surface geostrophic currents that use these SSH anomaly fields in their derivation. This conclusion is supported by analysis of the probability distribution functions (PDFs) of the FTLEs computed based on UPD and REF currents; computation of Eulerian and Lagrangian autocorrelations calculated using UPD and REF currents; inspection of the LCS patterns revealed in the FTLE fields computed using UPD and REF currents; analysis of the variance spectra of these FTLE fields; and explicit passive tracer advection calculations based on the UPD and REF currents. Calculations are carried out in an ample region of the western North Atlantic Ocean, which was considered in the study presented by Pascual et al. (2006), and over 2003, a year for which the UPD SSH anomaly field record includes information from four satellite altimeters.

Section 2 offers a description of the two different SSH anomaly fields considered in this work together with details of the construction of the total SSH fields employed in the Lagrangian calculations. This section also provides some specific details of the computation of FTLEs employed in the extraction of LCSs. In addition, numerical details of the computation of the various statistics considered are provided in this section. Section 3 presents the results from the FTLE computations and explicit passive tracer calculations. A summary and the conclusions of the study are presented in section 4. An appendix contains some mathematical details.

2. Methods

a. SSH and velocity fields

The two SSH anomaly fields distributed by AVISO employed in this work differ by the number of satellite altimeters involved in their construction (Ducet et al. 2000; Le Traon et al. 1998, 2003). One SSH anomaly field is tagged REF and is constructed using SSH anomaly measurements made using two altimeters with the same groundtracks [Ocean Topography Experiment (TOPEX)/Poseidon + European Remote Sensing Satellite (ERS) or *Environmental Satellite* (*Envisat*) + *Jason-1* or *Envisat* + *Jason-2*]. The other SSH anomaly field record is tagged

UPD, which is constructed using SSH anomaly measurements made using up to four satellite altimeters [TOPEX/Poseidon + *Envisat* + *Geosat Follow On* (*GFO*) + *Jason-1,* between October 2002 and September 2005 or *Envisat* + *GFO* + *Jason-1* + *Jason-2*, between June and November 2008]. While the sampling is improved in the UPD field, the quality of the series is not homogeneous as it is in the case of the REF field. These SSH anomaly field records are provided weekly on a 0.25°-resolution longitude–latitude grid and are referenced to a 7-yr (1993–99) mean.

The advection fields used in this study are given by surface geostrophic currents computed based on total SSH fields obtained by adding the above SSH anomaly fields to a 7-yr (1993–99) mean SSH field. The latter is given by a mean dynamic topography constructed based on altimetry and in situ measurements and a geoid model (Rio and Hernandez 2004). The position of a fluid particle on the ocean's surface is thus assumed to evolve according to

$$\dot{\lambda} = -\frac{g \sec\vartheta}{a^2 f(\vartheta)} \partial_\vartheta \eta(\lambda, \vartheta, t) \quad \text{and} \tag{1a}$$

$$\dot{\vartheta} = +\frac{g \sec\vartheta}{a^2 f(\vartheta)} \partial_\lambda \eta(\lambda, \vartheta, t). \tag{1b}$$

Here the overdot stands for time differentiation, λ (ϑ) denotes longitude (latitude), $\eta(\lambda, \vartheta, t)$ is the SSH, $f(\vartheta) = 2\Omega \sin\vartheta$ is the Coriolis parameter in which Ω is the earth's mean angular speed, a is the earth's mean radius, and g is gravity.

b. FTLEs and LCSs

From the aforementioned advection fields, LCSs are extracted by computing FTLEs. The (largest) FTLE is given by

$$\sigma_t^\tau(\mathbf{x}) := (2|\tau|)^{-1} \ln\lambda_{\max}[\Delta(\mathbf{x}; t, \tau)^{\mathrm{T}} \Delta(\mathbf{x}; t, \tau)], \tag{2a}$$

where $\lambda_{\max}$ stands for maximum eigenvalue and

$$\Delta(\mathbf{x}; t, \tau) := \mathsf{m}[\varphi_t^{t+\tau}(\mathbf{x})]^{1/2} \partial_x \varphi_t^{t+\tau}(\mathbf{x}) \mathsf{m}(\mathbf{x})^{1/2}. \tag{2b}$$

Here $\varphi_t^{t+\tau}$ is the flow map that takes a solution of the nonautonomous dynamical system (1) at time t to a solution at time $t + \tau$—that is,

$$\varphi_t^{t+\tau}:\mathbf{x}(t) = \begin{bmatrix} \lambda(t) \\ \vartheta(t) \end{bmatrix} \mapsto \mathbf{x}(t+\tau) = \begin{bmatrix} \lambda(t+\tau) \\ \vartheta(t+\tau) \end{bmatrix}; \tag{2c}$$

T denotes matrix transposition; and

$$\mathsf{m}(\mathbf{x}) := \begin{pmatrix} a^2 \cos^2\vartheta & 0 \\ 0 & a^2 \end{pmatrix} \tag{2d}$$

is the metric matrix, that is, the arclength element squared $ds^2 = a^2 \cos^2\vartheta\, d\lambda^2 + a^2\, d\vartheta^2 = d\mathbf{x}^{\mathrm{T}} \mathsf{m}(\mathbf{x})\, d\mathbf{x}$. A derivation of (2b) is given in the appendix; for an alternative one, which requires more advanced knowledge of differential geometry, see Lekien and Ross (2010).

In Shadden et al. (2005) it is demonstrated that the FTLE is approximately Lagrangian; that is, $\dot{\sigma}_t^\tau(\mathbf{x}) = O(|\tau|^{-1})$. Furthermore, Shadden et al. proved that the flux across a well-defined ridge of FTLE field, defined as a curve about which the FTLE falls off fastest, can be $O(|\tau|^{-1})$. The significance of the last property is that FTLE ridges are almost material fluid curves. On the other hand, the forward (backward) time separation rate of initially nearby fluid particles is maximal along a ridge of FTLE field computed in forward (backward) time; that is, with $\tau > 0$ ($\tau < 0$). Similar behavior is experienced along repelling (attracting) LCSs defined as the strongest local repelling (attracting) fluid curves (Haller and Yuan 2000). Thus, with some caveats (Branicki and Wiggins 2010; Haller 2002), FTLE ridges constitute quite good LCS indicators.

Focus in the present work is restricted to attracting LCSs, which delineate pathways for the evolution of passively advected tracers and, thus, are most insightful for the purpose of the present study.[2]

c. Computational details of FTLEs and other mixing diagnostics and additional data

The FTLE computations presented below are carried out by evaluating the derivatives in (2b) using finite differentiation over a 512 × 512 lattice of initial fluid particle positions regularly distributed over the region of the western North Atlantic spanning from 35° to 47°N, 51° to 39°W (Fig. 1, top). These computations have been chosen to be carried out over 2003, the year for which the construction of the UPD SSH anomaly field record includes information from four satellite altimeters. The particle trajectory integrations involved in the FTLE computations are carried out using a time-step-adapting fourth/fifth-order Runge–Kutta scheme. The required spatiotemporal interpolations are performed using a linear method. [Higher-order interpolation schemes (Lekien and Marsden 2005; Mancho et al. 2006) are in general required to produce accurate trajectory integrations, but

[2] In a Lagrangian coastal ocean study Shadden et al. (2009) found that focus on repelling LCSs was more appropriate. Beron-Vera et al. (2008) is an example of a Lagrangian ocean study based on the analysis of both attracting and repelling LCSs.

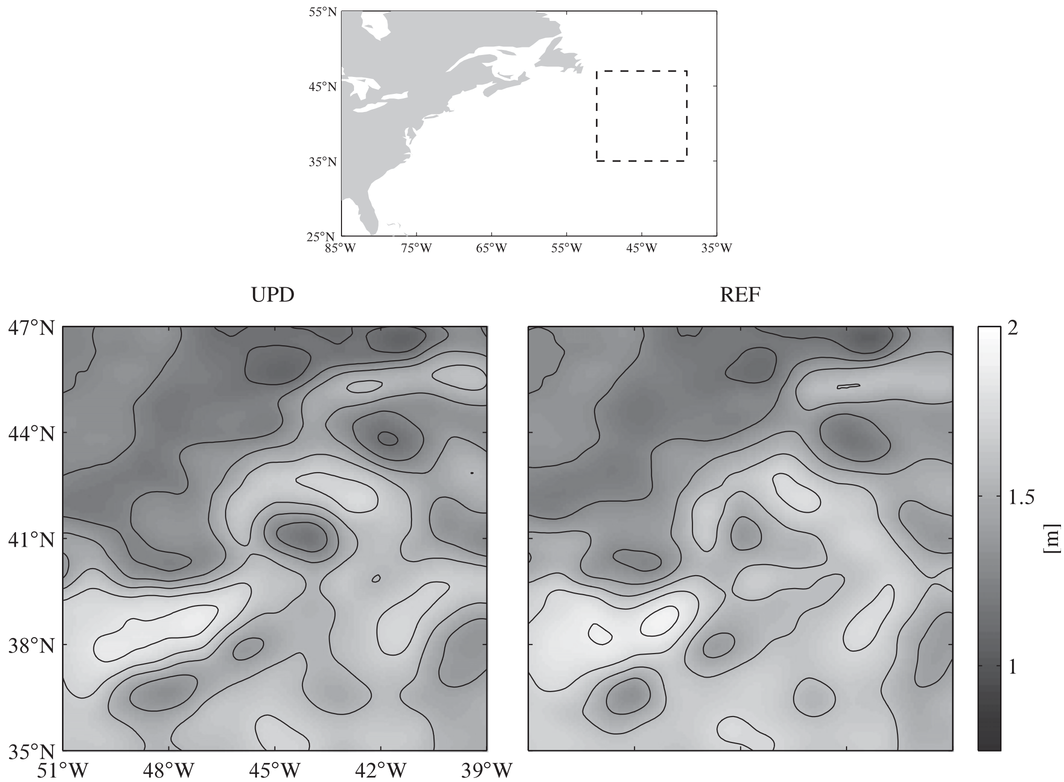

FIG. 1. (top) Map showing a portion of the western North Atlantic with the region of study indicated. (bottom) SSH field snapshots on 21 May 2003 extracted in the region of study, which result from the addition to a mean SSH field of SSH anomaly fields resulting from combined processing of measurements made by (left) four and (right) two satellite altimeters. The mean SSH field is a mean dynamic topography computed based on altimetry and in situ measurements and a geoid model. The two- and four-altimetry SSH anomaly fields are distributed by AVISO under the tags REF and UPD, respectively. Depicted SSH contours are 0.5–2 m in steps of 0.25 m.

this has not been found necessary here as in analyses (e.g., Beron-Vera and Olascoaga 2009; Beron-Vera et al. 2008) based on velocity fields similar to those considered in this work]. The choice $\tau = -30$ days is found sufficient to produce FTLE fields that unveil most of mesoscale LCSs as well LCSs below this scale. Longer time integration choices, for example, $\tau = -60$ days, as in Beron-Vera et al. (2008), result mainly in more detailed LCSs without substantially affecting their position. The position of the LCSs is not found to be substantially changed either if the metric is ignored in the FTLE calculation; that is, if $\mathsf{m}(\mathbf{x}) = \mathsf{Id}$ in place of (2d) is used in (2b). The latter is not a result of the relatively small meridional extension of the domain considered here, but rather of the boundedness of the entries of $\mathsf{m}(\mathbf{x})$ (Lekien and Ross 2010).

Probability distribution functions of FTLEs are computed to better understand implications for mixing. The study of the shape of the PDFs and their sensitivity, or lack thereof, to whether the FTLE is computed based on UPD or REF currents allows one to make inferences about the nature of mixing. The PDFs shown below correspond to normalized histograms constructed by binning FTLE records into equally spaced containers, counting the number of elements within each container, and normalizing such that the probability in the interval of interest equals unity.

One-dimensional spectrum computations are carried out to gain further insight into the FTLE calculations. These computations allow one to test the inferences made based on the analysis of the PDFs against known results from turbulence phenomenology. The computations are carried out as in Errico (1985) using a fast Fourier transform (FFT) by previously removing any linear trends from the FTLE fields inside the region of interest. This allows one to formally apply FFTs and also prevents the smaller unresolved scales from being aliased by larger unresolved scales. A one-dimensional spectrum is determined by first computing the corresponding two-dimensional spectrum using the FFT and then summing

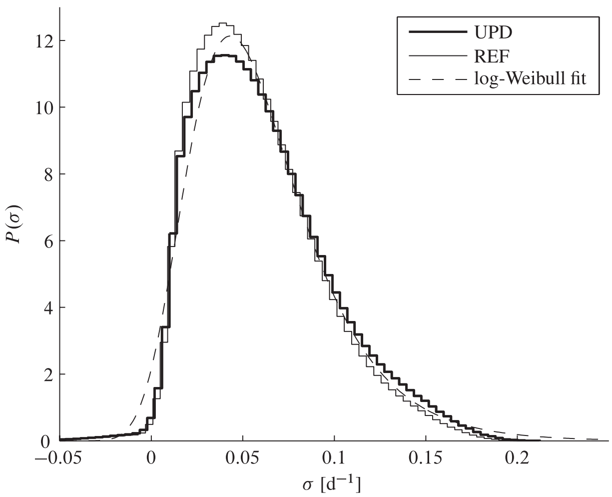

FIG. 2. Normalized PDFs of 30-day backward FTLEs computed weekly during 2003 based on UPD and REF currents in the domain shown in the top panel of Fig. 1. The UPD (REF) currents are derived geostrophically from SSH fields with UPD (REF) SSH anomalies.

the density within a discrete annulus in the two-dimensional wavenumber space, where a one-dimensional wavenumber is defined as the central radius of that annulus.

Finally, to study the validity of the FTLE calculations some FTLE fields are compared against satellite-tracked drogue drifter trajectory data. These data consist of daily drifter positions subsampled from raw drifter positions, previously low-pass filtered with a 5-day cutoff.

3. Results

The bottom-left panel (bottom-right panel) of Fig. 1 shows a snapshot of UPD (REF) SSH field on 21 May 2003 extracted in the region of study. Although the features seen in these SSH field snapshots are in general similar, they exhibit some differences: most notably, the depression roughly located near the center of the region, which occupies a larger area in the UPD field than in the REF field. Similar differences were pointed out by Pascual et al. (2006), who, as noted above, considered similar SSH field records as those considered here. The extent to which these differences have a substantial impact on mixing is investigated in the subsections that follow.

a. PDFs of FTLEs

Information on the nature of mixing can be extracted from the statistics of FTLEs. Figure 2 shows normalized PDFs of (backward) FTLEs, $P(\sigma)$, computed based on UPD and REF currents in the domain of study. Each PDF is constructed using a weekly record of FTLEs for the interval 1 January through 31 December 2003. The PDFs are very similar, both exhibiting a Gaussian core with a long tail toward large (backward time) stretching rates.

The non-Gaussian nature of the PDFs suggests that mixing is quite heterogeneous. To understand this, consider the case of a stationary stochastic system wherein trajectories randomly survey the entire phase space. In this case one expects the PDF to be a Gaussian, narrowing as the integration time increases and converging to a delta function at the LE in the infinite-time limit. For a system wherein both regular and irregular trajectories coexist, which means that trajectories cannot uniformly sample the phase space, the PDF cannot be expected to be Gaussian but rather multimodal, with each extremum roughly centered at the infinite-time LE within each irregular motion region. Thus, roughly speaking, the broader (narrower) the PDF, the more heterogeneous (homogeneous) the mixing (e.g., Shepherd et al. 2000). [Additional results on the relationship between PDFs of FTLEs and mixing properties can be found in Beigie et al. (1993), Liu et al. (1994), and Tomsovic and Lakshminarayan (2007).]

Similar non-Gaussian FTLE statistics were reported in global (Beron-Vera et al. 2008; Waugh and Abraham 2008) and regional (Abraham and Bowen 2002; Rossi et al. 2009; Waugh et al. 2006) ocean studies based on UPD currents. The PDFs shown in Fig. 2 are fairly well fitted by a log–Weibull model,

$$P(\sigma) \sim \frac{1}{A}\exp\frac{A-\sigma}{B}\exp\left(-\exp\frac{A-\sigma}{B}\right), \tag{3}$$

where $A \approx 0.03$ day^{-1} and $B \approx 0.02$ day^{-1}. A fit similar to (3) that captures the strongly skewed nature of the PDFs toward large stretching rates has been proposed and argued to be universal (Waugh and Abraham 2008). The differences between fit (3) and the one in Waugh and Abraham (log–Weibull versus Weibull) are attributed to differences in the FTLE calculations. Unlike the FTLEs computed by Waugh and Abraham (2008), the FTLEs as computed here are not enforced to be nonnegative. As a result, small tails toward negative FTLE values are seen in the PDFs depicted in Fig. 2, which explain the differences in the fits (only in the strictly nondivergent velocity field case on a Cartesian plane these tails can be guaranteed to be absent because the sum of the largest and smallest FTLEs must vanish).

The reported close similarity of the PDFs of FTLEs computed using UPD and REF currents suggests that the differences between the SSH anomaly records employed in their construction have a small impact on mixing. In other words, mixing as sustained by altimetry-derived currents appears to be largely insensitive to their resolution. It must be noted, however, that UPD currents actually have the same spatiotemporal resolution as REF currents. However, they differ as a result of the consideration of different amounts of altimetric measurements in the SSH anomaly fields employed in their construction. These differences nevertheless play a similar role as the differences between a given velocity field and that corresponding to a truncation in space and/or time of the latter. Resolution-independent mixing is consistent with the notion of "chaotic mixing" but is inconsistent with the notion of "turbulent mixing" (Shepherd et al. 2000). Chaotic mixing refers to a situation wherein the advection field is spatially quasi coherent and temporally quasi regular on time scales over which the fluid particle motion is predominantly irregular; in contrast, turbulent mixing refers to a situation wherein both the velocity field is spatiotemporally incoherent and the fluid particle motion is irregular (Brown and Smith 1991; Shepherd et al. 2000; Swanson and Pierrehumbert 1997). The analyses presented below are aimed at providing support to the idea that mixing as sustained by altimetry-derived currents is most easily described as being chaotic than turbulent.

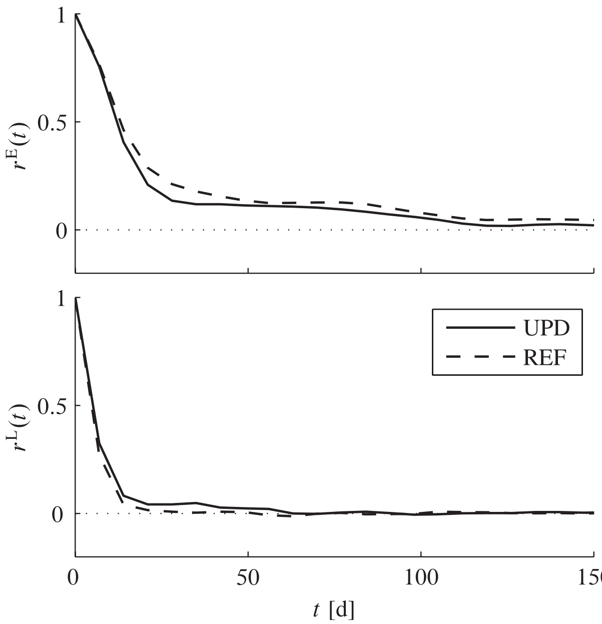

FIG. 3. (top) Eulerian and (bottom) Lagrangian autocorrelation function estimates based on UPD and REF currents.

b. *Eulerian versus Lagrangian correlation times*

We start by considering Eulerian and Lagrangian autocorrelations of velocity derivatives [or derivatives of the rhs of (1) to be more precise]. The latter control relative dispersion of fluid particles, and thus inspection of their autocorrelations allows one to make inferences about the persistence of the strain field.

Given a function $q(t)$ on the interval $t \in [0, T]$, the lag-μ autocorrelation $r(\mu)$ is given by

$$r(\mu) := \frac{\dfrac{1}{T-\mu}\displaystyle\int_0^{T-\mu} [q(t) - \overline{q}][q(t+\mu) - \overline{q}]\,dt}{\dfrac{1}{T}\displaystyle\int_0^{T} [q(t) - \overline{q}]^2\,dt}, \quad (4)$$

where $\overline{q} = T^{-1}\int_0^T q(t)\,dt$. An Eulerian autocorrelation is obtained when $q(t)$ is the time series that results from evaluating a certain variable $Q(x, t)$ at a fixed location x_0; that is, $Q(x_0, t) = q(t)$. A Lagrangian autocorrelation is obtained when $q(t)$ is the time series that results from evaluating $Q(x, t)$ along the trajectory $\varphi_{t_0}^t(x_0)$ of a fluid particle that at time t_0 was located at x_0; that is, $Q[\varphi_{t_0}^t(x_0), t] = q(t)$.

Figure 3 shows Eulerian, $r^E(\mu)$, and Lagrangian, $r^L(\mu)$, autocorrelation curves of the derivative in the (nearly) along Gulf Stream direction of the velocity in the same direction (other velocity derivatives produce similar results). Each curve shown in the figure corresponds to an average over an ensemble of autocorrelation curves computed over 2003. The Eulerian and Lagrangian autocorrelation curves inferred using UPD and REF currents are nearly identical, both exhibiting an approximately exponential decay with time. The Lagrangian autocorrelation is effectively zero after 60 days, whereas the Eulerian autocorrelation decreases much more slowly and is not seen to vanish even after 150 days. Hence there seems to be a finite Lagrangian autocorrelation time and an undetermined (or at least a fairly much longer) Eulerian autocorrelation time (estimated e-folding time scales are 5 days for the Lagrangian autocorrelation and 15 days for the Eulerian autocorrelation). This suggests that the Lagrangian evolution is more irregular than the driving Eulerian flow and, hence, that altimetry-derived currents sustain mixing that can be more fairly characterized as being chaotic than turbulent.

c. *Inspection of LCS patterns*

We now turn to the qualitative analysis of (attracting) LCSs, which, as noted above, control the evolution of passively advected tracers. The right (left) panel of Fig. 4 shows a snapshot of the FTLE field on 21 May 2003 computed based on UPD (REF) surface geostrophic currents. Negative FTLE values are not shown in the figure to allow for a better identification of LCSs (these values, however, tend to occur only in very localized regions). LCSs roughly correspond to the highly convoluted narrow bands of brightest white tones in each panel. Note the rich variety of features revealed. It is important to note that the scales of theses features are not constrained by the spatial resolution scale of the velocity field, which is ~35 km. The FTLEs can be, and

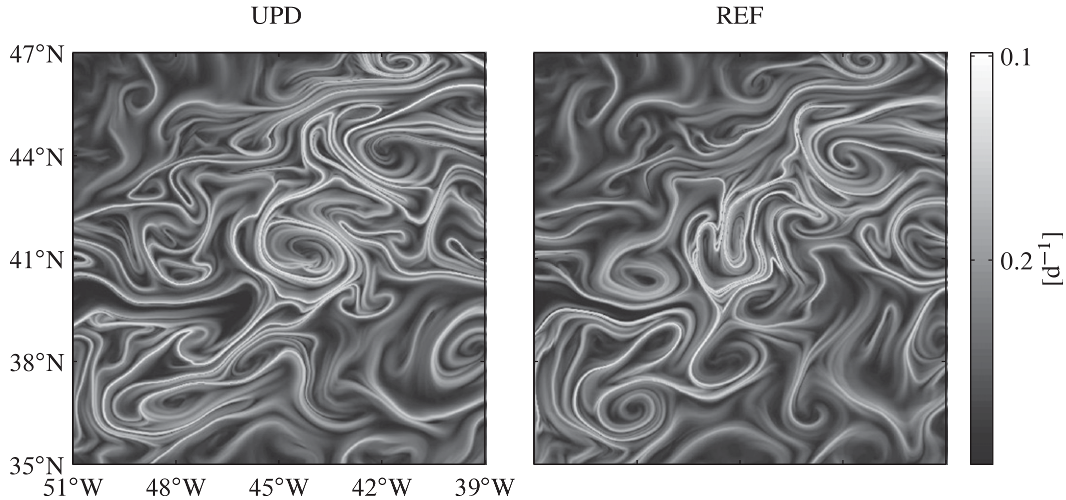

FIG. 4. FTLE field snapshot on 21 May 2003 computed based on (left) UPD and (right) REF currents. LCSs are identified with locally maximizing curves or ridges of the FTLE field. These roughly correspond to the highly convoluted narrow bands of brightest white tones in each panel.

have been, calculated on a grid finer than that the one on which the velocity field is defined. Here such a calculation is carried out on an ~0.025° resolution grid, which is 10 times finer than that one on which the velocity field is defined. The figure reveals filaments whose widths can be <35 km, which wrap around themselves. The fine texture of the resulting LCS pattern is characteristic of chaotic mixing; this contrasts with turbulent mixing in whose case the associated LCS pattern is characterized by substantial small-scale wiggling (Bartello 2000). The features revealed in the figure are not apparent in, and cannot be guessed from, the corresponding SSH fields shown for the same date in the bottom panels of Fig. 1. Consistent with the analysis of the PDFs of FTLEs, the main traits of the LCS pattern produced by UPD currents are captured by that produced by REF currents. Only details of this pattern are different. For instance, details of the dipolar vortex, identified with a mushroom-like LCS near the center of the domain, are different. The noted differences can only produce differences on the deterministic calculation of the trajectory of a particular fluid particle. However, because the noted differences are not too large either, the statistics of mixing are not expected to be impacted substantially. This is consistent with the above analysis of PDFs of FTLEs and Eulerian and Lagrangian autocorrelations and is further supported by the analysis of additional mixing diagnostics presented below.

d. Comparison with drifter trajectory data

Before turning to the analysis of additional mixing diagnostics, the validity of the FTLE computations is assessed by comparing the trajectory of a satellite-tracked drifter with the evolution of the LCSs extracted from UPD (Fig. 5, top two rows) and REF (Fig. 5, bottom two rows) currents. The evolution of the LCSs is manifested in the change of position and shape of the ridges in the FTLE fields (in grayscale), which are shown every two days during the entire tracking interval of the drifter. The drifter's instantaneous position is indicated by a yellow dot with a red border; the yellow curve represents the drifter's past trajectory. For the case of UPD currents the agreement between the drifter's change in position and LCS deformation is remarkably good, despite that UPD currents are coarse, purely geostrophic currents (e.g., Ekman drift effects are not considered here). In fact, on 14 May 2003 the drifter is seen to lie well within the core of the cyclonic vortex (the LCS filaments wrap around clockwise) that compose the dipolar vortex sustained by UPD currents discussed in section 3c. At all times shown the drifter position falls well inside this cyclonic vortex, which propagates westward. Moreover, the drifter is not only seen to lie well inside the cyclonic vortex at all times shown but also to nearly follow the evolution of the LCSs that define this vortex. For the case of REF currents, the agreement between the drifter's change in position and LCS evolution cannot be claimed to be so good. The disparities in this case are consistent with the noted discrepancies between details of the LCSs extracted from UPD and REF currents, which constrain the ability of REF currents, with respect to that of UPD currents, to produce deterministic passive tracer advection calculations.

The entire trajectory of the same drifter considered here is compared in Pascual et al. (2006) with two instantaneous SSH field snapshots, one constructed using

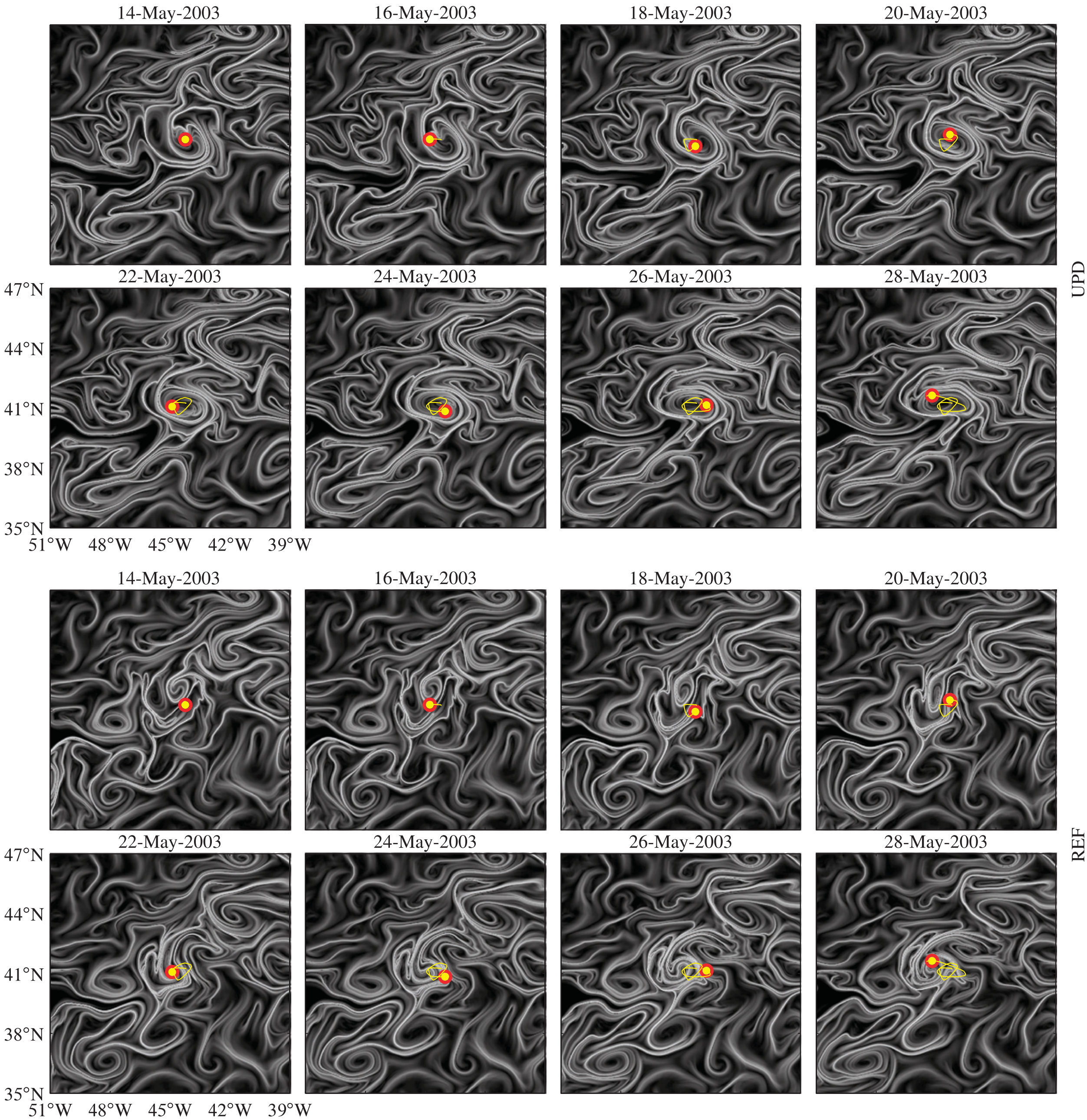

FIG. 5. Sequence of selected snapshots of FTLE field computed based on (top) UPD and (bottom) REF currents (grayscale) with the instantaneous position (yellow dot with red border) and past trajectory (yellow curve) of a satellite-tracked drogue drifter overlaid.

SSH anomalies that involved measurements acquired by four altimeters and the other using SSH anomalies that used measurements taken by two altimeters. That comparison is presented in support of the conclusion that currents can be better inferred using the SSH anomalies that include measurements from more altimeters. It might be argued that, during the relatively short time interval over which the drifter's position is tracked, the altimetry-derived currents are approximately steady, thereby justifying the comparison made by Pascual et al. However, Fig. 5 reveals that the deformation experienced by the LCSs is not negligible, thereby making the comparison of the drifter trajectory with SSH contours inappropriate.

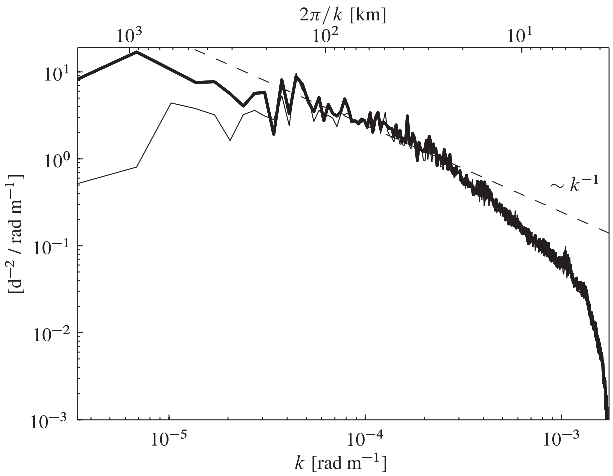

FIG. 6. Variance spectrum estimate of the difference between FTLEs computed using UPD and REF currents (thin curve) and of FTLEs computed using UPD currents (bold curve) on 21 May 2003 as a function of total horizontal wavenumber. The dashed curve, shown for reference, is labeled by its wavenumber dependence.

e. Spectra of FTLEs

The differences between the LCS patterns supported by UPD and REF currents are now analyzed in more detail. This is done as in Bartello (2000) by considering the variance spectrum of the difference between the FTLE fields computed using UPD and REF currents. Let $\theta_1(x)$ and $\theta_2(x)$ be any two fields and define the variance spectrum of each field and of their difference, respectively, by the following relationships:

$$\frac{1}{2}\langle\theta_n(x)^2\rangle =: \int E_{\theta_n}(k)\,dk, \quad n = 1, 2, \quad \text{and} \tag{5}$$

$$\frac{1}{4}\langle[\theta_1(x) - \theta_2(x)]^2\rangle =: \int E_{\delta\theta}(k)\,dk, \tag{6}$$

where the angle bracket denotes average and k is the total wavenumber. If $\theta_1(x)$ and $\theta_2(x)$ are completely decorrelated ($\langle\theta_1\theta_2\rangle = 0$) but have the same variance ($\langle\theta_1^2\rangle = \langle\theta_2^2\rangle$), then $E_{\theta_1} = E_{\theta_2} = E_{\delta\theta}$, which indicates a total lack of "forecast skill" of one variable with respect to another. Figure 6 shows numerical estimates of the variance spectrum of the differences between the FTLE fields computed using UPD and REF currents (thin curve) and of the FTLE field computed using UPD currents (bold curve) on 21 May 2003. Note that the error committed by making passive tracer calculations based on REF currents with respect to UPD currents decreases with increasing length scales and is important for length scales below roughly 110 km. This length scale, however, seems to be somewhat larger than that one that may be inferred from visual comparison of the LCS patterns extracted from UPD and REF currents.

Consistent with the notion discussed above that passive tracer mixing is dominated by chaotic mixing, the slope of the variance spectrum of the FTLE field is computed using UPD currents $\alpha \approx -1$ or greater above roughly 20 km. To understand this, recall that the FTLE behaves almost as a passive tracer, which allows one to attempt applying two-dimensional turbulence phenomenology (Batchelor 1959; Kraichnan 1971; Obhukov 1949). The latter supports the notion that, if $\alpha = -1$, then there exists a single characteristic time scale of tracer variance transfer, which is set by the large-scale components of the velocity field. As a consequence, passive tracer evolution at a given scale is governed by velocity field features at a larger scale (Babiano et al. 1985). This passive tracer evolution regime is referred to as spectrally nonlocal, which contrasts with the spectrally local regime wherein passive tracer evolution at a given scale is governed by velocity field features at a comparable scale (Bennett 1984). Chaotic mixing can be seen as a special case of spectrally nonlocal dynamics, whereas it is not consistent with spectrally local dynamics. In terms of the kinetic energy spectral slope, say β, the spectrally nonlocal regime is characterized by a steep slope ($\beta < -3$), whereas the spectrally local regime is characterized by a more gentle slope ($\beta > -3$). According to two-dimensional turbulence phenomenology, the present FTLE calculations suggest $\beta \approx -3$ or smaller above roughly 20 km. This is partly verified by computations of kinetic energy spectra (not shown), which suggest $\beta < -3$ for length scales larger than roughly 50 km (below that scale no reliable information can be extracted because the velocity field resolution scale is approximately 35 km). This result is consistent with recent computations (Isern-Fontanet et al. 2006) that suggest $\beta < -3$ based on the analysis of altimetric SSH maps. Also, it is partly consistent with earlier calculations (Stammer 1997; Stewart et al. 1996) of kinetic energy spectra inferred from variance spectra of altimetric SSH anomaly measurements along groundtracks, which suggested that $\beta \approx -3$ for length scales O(10–500 km). However, recent similar computations (Le Traon et al. 2008) seem to suggest that $\beta > -3$. It must be noted that Armi and Flament (1985) have made some cautionary remarks about the spectral interpretation of mixing regimes, which demands the analysis of other diagnostics for their interpretation as is done here.

f. Passive tracer advection calculations

Passive tracer advection experiments are described now that consist in tracking the evolution of a circular-shaped tracer patch composed of 10^6 marked (synthetic)

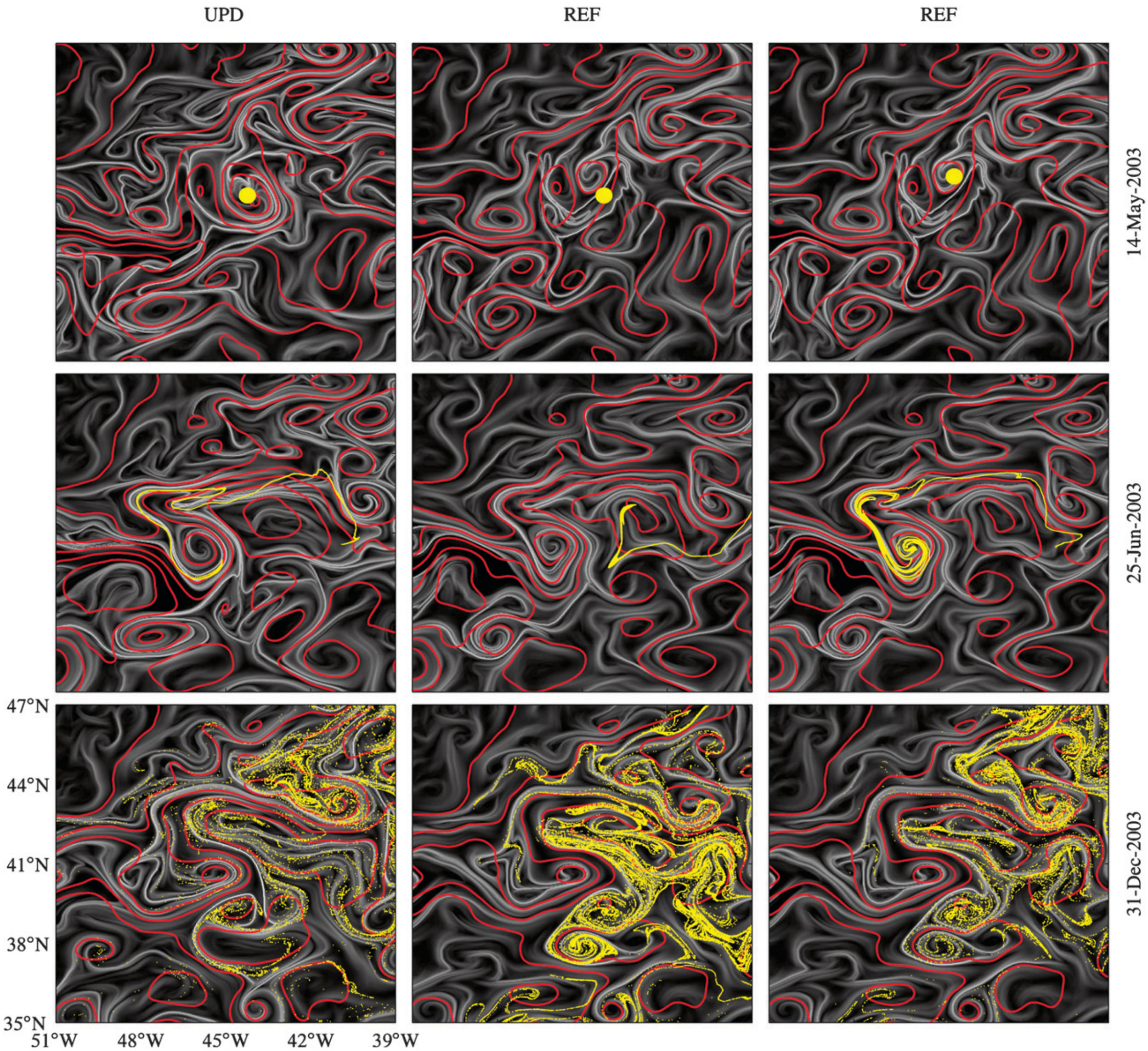

FIG. 7. Sequence of selected snapshots of the evolution of a passive tracer patch (yellow dots) for calculations based on UPD and REF currents. On each date shown, the passive tracer patch is depicted overlaid on the corresponding FTLE field distribution (grayscale) and SSH field selected contours (red curves). The passive tracer patch on 14 May 2003 takes a circular shape and is composed of 10^6 marked (synthetic) fluid particles. Note that the center of the initially circular passive tracer patch for the evolution labeled REF-b is slightly displaced with respect to that for the evolutions labeled UPD and REF-a.

fluid particles as advected by UPD (Fig. 7, left) and REF (Fig. 7, middle and right) currents. The positions of the fluid particles on each date are depicted (in yellow) overlaid on the corresponding FTLE field distribution (in grayscale) and SSH field selected contours (in red). For evolutions shown in the left and middle panels (referred to as UPD and REF-a) the center of the circular tracer patch is chosen to be located on 14 May 2003 near the core of the cyclonic vortex that conforms to the dipolar vortex sustained by UPD currents, discussed in section 3c. For the evolution shown in the right panels (referred to as REF-b) the center of the circular tracer patch is chosen to lie on the same date near the core of the cyclonic vortex that compose the dipolar vortex sustained by REF currents, also discussed in section 3c. Several points are noteworthy. First, independent of whether advection is provided by either UPD or REF currents and of the initial condition, the tracer evolves very tightly following the evolution of the LCSs. This explicitly demonstrates that the LCSs demarcate pathways for the evolution of passively advected tracers. Second, consistent with the fine texture of the features that characterize the LCS patterns, tracer evolution takes on similar fine textured patterns, which are characteristic of chaotic mixing. Third, although the closed SHH contours that surround the tracer patches on 14 May 2003 for evolutions UPD and REF-b propagate primarily westward, a large number of tracers is ejected outside the SSH contours and transported mainly in an eastward direction. Thus, vortices, defined by closed SSH contours (streamlines) in a reference frame attached to the earth, cannot always be claimed to constitute traps that transport slugs of fluid over distances as large as commonly assumed (e.g., Goni and Johns 2001; Witter and Gordon 1999). Fourth, evolutions UPD, REF-a, and REF-b are not seen to be identical but still have qualitatively similar traits. The differences are consistent with the noted disparities in the details of the LCS patterns, which suggested that deterministic passive tracer advection calculations based on UPD and REF currents should not be identical. The qualitative similarities are consistent with the noted close resemblance between the PDFs of FTLEs computed based on UPD and REF currents, which suggested that the statistics of mixing should be similar. Fifth, the differences in the tracer distributions when advection is supplied by UPD and REF currents can be substantially narrowed by appropriately choosing the initial position of the tracer patch. This clearly follows from the comparison of evolutions UPD and REF-b.

In support of the third through fifth points above, Fig. 8 shows time series of the percentage of marked fluid particles found inside, north, south, east, and west of the domain where evolutions UPD, REF-a, and REF-b depicted in Fig. 7 take place. A common feature of all evolutions is that after a year or so most of the tracer has left the domain. The escape rate is similar for evolutions UPD and REF-b, both being faster than that for evolution REF-a. In exiting the domain the tracer takes a mostly east-northeastward path for evolutions UPD and REF-b, while a mainly east-southeastward path for evolution REF-a. The escape rates through the northern and eastern boundaries are similar for evolutions UPD and REF-b, with the escape rate through the eastern boundary being larger than that through the northern boundary. The escape rate through the southern boundary is smaller than that through the eastward boundary for evolution REF-a, with the escape rate through the eastern boundary, albeit considerable, being smaller than that for either evolution UPD or REF-b.

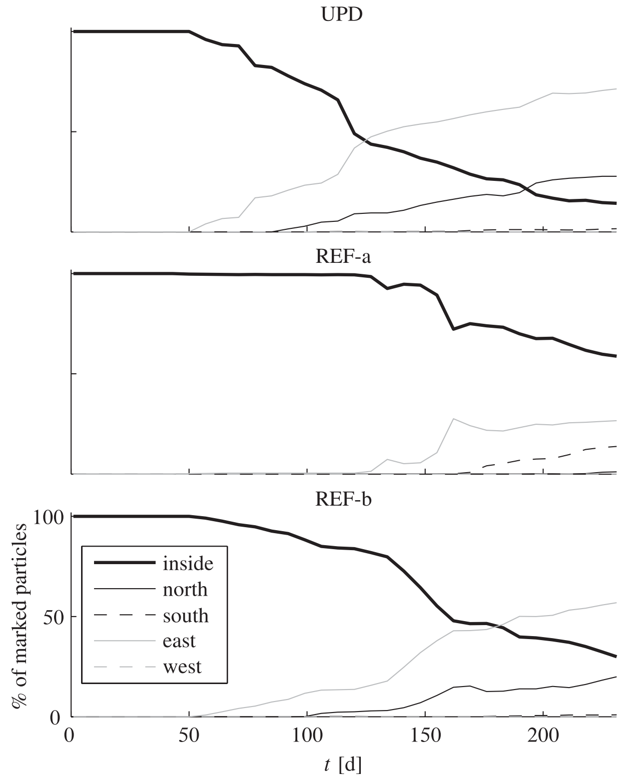

FIG. 8. Time series starting on 14 May 2003 of percentage of marked fluid particles lying inside, north, south, east, and west of the domain spanning 35°–47°N, 51°–39°W for marked fluid particles whose evolutions within this domain are shown in Fig. 7 under labels UPD, REF-a, and REF-b.

4. Summary and conclusions

We have investigated the effects on surface ocean mixing of the differences between two altimetry products distributed by AVISO. One product, tagged REF, is given by a sea surface height (SSH) anomaly field constructed using measurements made by two satellite altimeters. The other product, tagged UPD, is given by an SSH anomaly field built using measurements made by up to four satellite altimeters. Focus in this work was placed on a region of the western North Atlantic in 2003, the year for which the UPD product includes information from four satellite altimeters. The same region in 2003 was considered in a recent assessment of the differences between SSH anomaly field records similar to those considered here. The present assessment extended that study by taking into consideration implications for mixing with an emphasis on the extraction of Lagrangian coherent structures (LCSs).

Hidden in the flow, LCSs are the strongest local attracting or repelling material fluid curves. As such, LCSs compose the backbone of the Lagrangian circulation; that is, they entirely control the mixing of passively advected tracers. Attracting LCSs, in particular, supply a theoretical sustain for the filaments often observed in distributions of tracers passively advected by unsteady velocity fields. This type of LCSs was here extracted from surface geostrophic currents computed using the above two SSH anomalies superimposed on a mean SSH field resulting from the combined use of altimetry and in situ measurements and a geoid model. Ridges of finite-time (backward) Lyapunov exponents (FTLEs) were employed as LCS detectors.

The main traits of the LCS patterns produced by currents derived using UPD and REF SSH anomalies (UPD and REF currents, respectively) were found to be generally quite similar. This finding was found consistent with the analysis of the probability distribution functions (PDFs) of FTLEs computed using UPD and REF currents. The PDFs were found to be very similar, both being strongly skewed toward large (backward time) stretching rates and suggesting highly heterogeneous mixing. The observed similarity of the PDFs suggested resolution-independent mixing, consistent with a regime dominated by chaotic mixing, as opposed to turbulent mixing. This notion was supported by the slower decay rate of Eulerian autocorrelations compared to Lagrangian autocorrelations. The fine textured patterns formed by the computed LCSs further supported the notion that chaotic mixing plays a dominant role. The results from explicit passive tracer advection calculations served to illustrate how the deformation of LCSs over time controls the evolution of a passive tracer patch. Consistent with the differences in the details of the LCS patterns, the distributions acquired by a given tracer patch while advected by UPD and REF currents also showed differences, which were narrowed by an appropriate choice of the initial position of the tracer patch. This was possible because the most salient features of the LCS patterns extracted from UPD currents, albeit distorted, were found to be present in those extracted from REF currents. Contrary to popular wisdom, the tracer calculations provided a demonstration for the fact that closed SSH contours do not generally constitute traps for passive tracers. A comparison of the evolution of the computed LCSs over time with the change in position of a satellite-tracked drifting buoy was also offered. This provided support for the results from the FTLE computations, which were found to be consistent with prior FTLE calculations based on UPD currents in regions of the World Ocean and time spans different than those considered here.

A main conclusion of this study is that the differences between the REF and UPD SHH anomaly field records have a small impact on the statistics of surface ocean mixing as supported by surface geostrophic currents that use these SSH anomaly field records in their construction. No attempt was made to make inferences about the effects of the scales not resolved by UPD currents, except that the extracted LCSs showed consistency with the trajectory of a satellite-tracked drifting buoy over a relatively short period of time (roughly 30 days). Consistent with recent studies on the effects of those unresolved scales on surface ocean mixing (e.g., Capet et al. 2008; Klein and Lapeyre 2009; Mahadevan and Tandon 2006), surface geostrophic currents produced by a high-resolution global general circulation ocean model suggest that surface ocean mixing may be more homogeneous than expected from current low-resolution groundtrack altimetry (Beron-Vera 2010). Validation of this result, however, demands appropriate measurements, which may be supplied by next-generation high-resolution wide-swath altimetry.

Acknowledgments. Technical assistance by P. DiNezio is sincerely appreciated. The comments made by two anonymous reviewers contributed to improve the manuscript. The altimeter products used in this work are produced by SSALTO/DUCAS and distributed by AVISO, with support from CNES (available online at http://www.aviso.oceanobs.com/duacs). The Rio05 product is produced by CLS Space Oceanography Division and is distributed by AVISO, with support from CNES (available online at http://www.aviso.oceanobs.com). The drifter trajectory data are distributed by the NOAA/AOML Drifter Data Assembly Center (available online at http://www.aoml.noaa.gov/phod/dac). FJBV and MJO were supported by NSF Grant CMG0825547 and NASA Grants NNX09AD82G and NNX10AE99G. GJG was supported by NASA Grants NNX09AD82G and NNX10AE99G and the NOAA/CPO.

APPENDIX

Computation of FTLEs on Non-Cartesian Phase Spaces

Let $\{x^i\}$, $i = 1, \ldots, n$, be the coordinates, not necessarily orthogonal, of point $\mathbf{x}$ on an n-space $\mathcal{S}$ on which the arclength element squared $ds^2 = d\mathbf{x}^{\mathrm{T}}\mathbf{m}(\mathbf{x})/d\mathbf{x}$, where $\mathbf{m}(\mathbf{x})$ is a symmetric and positive-definite matrix and $\mathbf{x} = (x^i)$ is understood as a column vector.[A1] The norm induced by this metric $\|\mathbf{a}\|_{\mathbf{x}} = [\mathbf{a}^{\mathrm{T}}\mathbf{m}(\mathbf{x})\mathbf{a}]^{1/2}$ for any vector $\mathbf{a}$; in particular, $\|d\mathbf{x}\|_{\mathbf{x}} = ds$. If $\mathcal{S}$ is the Cartesian n space, that is, $\mathcal{S} = \mathbb{R}^n$, then $ds^2 = d\mathbf{x}^{\mathrm{T}}d\mathbf{x}$; that is, $\mathbf{m}(\mathbf{x}) = \mathbf{Id}$.

Assume now that $\mathcal{S}$ constitutes the phase space of a nonautonomous dynamical system, which is given by

[A1] More precisely, $\mathcal{S}$ is an n manifold (i.e., diffeomorphisms exist between open subsets of $\mathcal{S}$ and $\mathbb{R}^n$ that completely cover $\mathcal{S}$), which is endowed with a Riemannian metric.

$$\dot{\mathbf{x}} = \mathbf{X}(\mathbf{x}, t) \tag{A1}$$

for a certain time-dependent vector field $\mathbf{X}(\mathbf{x}, t)$. Let

$$\varphi_t^r : \mathcal{S} \to \mathcal{S}; \quad \mathbf{x}(t) \mapsto \mathbf{x}(r) \tag{A2}$$

be the flow map. The FTLE,

$$\sigma_t^r(\mathbf{x}) := \frac{1}{|\tau|} \ln \max_{\mathbf{u} \neq 0} \frac{\|\delta\varphi_t^{t+\tau}(\mathbf{x}; \mathbf{u})\|_{\varphi_t^{t+\tau}(\mathbf{x})}}{\|\mathbf{u}\|_x}, \tag{A3}$$

where $\varphi_t^{t+\tau}(\mathbf{x}+\mathbf{u}) - \varphi_t^{t+\tau}(\mathbf{x}) = \delta\varphi_t^{t+\tau}(\mathbf{x}; \mathbf{u}) + O(\|\mathbf{u}\|_\mathbf{x}^2) = \partial_\mathbf{x}\varphi_t^{t+\tau}(\mathbf{x})\mathbf{u} + O(\|\mathbf{u}\|_\mathbf{x}^2)$ as $\|\mathbf{u}\|_\mathbf{x} \to 0$. The goal is to determine $\mathbf{\Delta}(\mathbf{x}; t, \tau)$ such that (A3) reduces to (2a).

Since $\mathsf{m}(\mathbf{x})$ is real and symmetric,

$$\mathsf{m}(\mathbf{x}) = \mathsf{V}(\mathbf{x})\mathsf{D}(\mathbf{x})\mathsf{V}(\mathbf{x})^\mathrm{T}. \tag{A4}$$

Here $\mathsf{D}(\mathbf{x}) = \mathrm{diag}[\lambda_i(\mathsf{m}(\mathbf{x})]$ and $\mathsf{V}(\mathbf{x}) = [\mathbf{v}_1(\mathbf{x}), \ldots, \mathbf{v}_n(\mathbf{x})]$, where $\mathsf{m}(\mathbf{x})\mathbf{v}_i(\mathbf{x}) = \lambda_i[\mathsf{m}(\mathbf{x})]\mathbf{v}_i(\mathbf{x})$ with $\{\mathbf{v}_i(\mathbf{x})\}$ spanning an orthogonal basis. Noting that $\mathsf{D}(\mathbf{x}) = \mathsf{D}(\mathbf{x})^{1/2}\,\mathsf{D}(\mathbf{x})^{1/2}$, one can then write

$$\|\mathbf{u}\|_\mathbf{x}^2 = \mathbf{u}^\mathrm{T}\mathsf{m}(\mathbf{x})\mathbf{u} \tag{A5a}$$

$$= \mathbf{u}^\mathrm{T}\mathbf{u}\mathsf{V}(\mathbf{x})\mathsf{D}(\mathbf{x})\mathsf{V}(\mathbf{x})^\mathrm{T}\mathbf{u} \tag{A5b}$$

$$= \tilde{\mathbf{u}}(\mathbf{x}; \mathbf{u})^\mathrm{T}\tilde{\mathbf{u}}(\mathbf{x}; \mathbf{u}), \tag{A5c}$$

where

$$\tilde{\mathbf{u}}(\mathbf{x}; \mathbf{u}) := \mathsf{D}(\mathbf{x})^{1/2}\mathsf{V}(\mathbf{x})^\mathrm{T}\mathbf{u}. \tag{A5d}$$

Similarly,

$$\|\delta\varphi_t^{t+\tau}(\mathbf{x}; \boldsymbol{u})\|_{\varphi_t^{t+\tau}(\mathbf{x})}^2 = \delta\varphi_t^{t+\tau}(\mathbf{x})^\mathrm{T}\mathsf{m}[\varphi_t^{t+\tau}(\mathbf{x})]\delta\varphi_t^{t+\tau}(\mathbf{x}) \tag{A6a}$$

$$= \tilde{\mathbf{u}}(\mathbf{x}; \mathbf{u})^\mathrm{T}\Delta(\mathbf{x}; t, \tau)^\mathrm{T}\Delta(\mathbf{x}; t, \tau)\tilde{\mathbf{u}}(\mathbf{x}; \mathbf{u}), \tag{A6b}$$

where

$$\Delta(\mathbf{x}; t, \tau) := \mathsf{D}[\varphi_t^{t+\tau}(\mathbf{x})]^{1/2}\mathsf{V}[\varphi_t^{t+\tau}(\mathbf{x})]^\mathrm{T}\partial_\mathbf{x}\varphi_t^{t+\tau}(\mathbf{x}) \times [\mathsf{D}(\mathbf{x})^{1/2}\mathsf{V}(\mathbf{x})^\mathrm{T}]^{-1}, \tag{A6c}$$

which is the form of the sought matrix as it follows from

$$\max_{\mathbf{a} \neq 0} \frac{\mathbf{a}^\mathrm{T}\mathsf{A}\mathbf{a}}{\mathbf{a}^\mathrm{T}\mathbf{a}} = \lambda_{\max}(\mathsf{A}) \tag{A7}$$

for any matrix A.

Finally, when the coordinates of the phase space are orthogonal, such as the geographic coordinates (λ, ϑ) on a sphere of radius a as considered in this work, the metric matrix $\mathsf{m}(\mathbf{x})$ has diagonal form [cf. (2d)]. In this case, $\mathsf{D}(\mathbf{x}) = \mathsf{m}(\mathbf{x})$ and $\mathsf{V}(\mathbf{x}) = \mathsf{Id}$, which reduces (A6c) to (2b).

REFERENCES

Abraham, E. R., and M. M. Bowen, 2002: Chaotic stirring by a mesoscale surface-ocean flow. *Chaos,* **12,** 373–381.

Armi, L., and P. Flament, 1985: Cautionary remarks on the spectral interpretation of turbulent flows. *J. Geophys. Res.,* **90,** 11 779–11 782.

Babiano, A., C. Basdevant, and R. Sadourny, 1985: Structure functions and dispersion laws in two-dimensional turbulence. *J. Atmos. Sci.,* **42,** 941–949.

Bartello, P., 2000: Using low-resolution winds to deduce fine structure in tracers. *Atmos.–Ocean,* **38,** 303–320.

Batchelor, G. K., 1959: Small-scale variation of convected quantities like temperature in turbulent fluid. Part 1, General discussion and the case of small conductivity. *J. Fluid Mech.,* **5,** 113–133.

Beigie, D., A. Leonard, and S. Wiggins, 1993: Statistical relaxation under nonturbulent chaotic flows: Non-Gaussian high-stretch tails of finite-time Lyapunov exponent distributions. *Phys. Rev. Lett.,* **70,** 275–278.

Bennett, A. F., 1984: Relative dispersion: Local and nonlocal dynamics. *J. Atmos. Sci.,* **41,** 1881–1886.

Beron-Vera, F. J., 2010: Mixing by low- and high-resolution surface geostrophic currents. *J. Geophys. Res.,* **115,** C10027, doi:10.1029/2009JC006006.

——, and M. J. Olascoaga, 2009: An assessment of the importance of chaotic stirring and turbulent mixing on the west Florida shelf. *J. Phys. Oceanogr.,* **39,** 1743–1755.

——, ——, and G. J. Goni, 2008: Oceanic mesoscale eddies as revealed by Lagrangian coherent structures. *Geophys. Res. Lett.,* **35,** L12603, doi:10.1029/2008GL033957.

——, ——, M. G. Brown, H. Koçak, and I. I. Rypina, 2010: Invariant-tori-like Lagrangian coherent structures with application to geophysical flows. *Chaos,* **20,** 017514, doi:10.1063/1.3271342.

Boffetta, G., G. Lacorata, G. Redaelli, and A. Vulpiani, 2001: Detecting barriers to transport: A review of different techniques. *Physica D,* **159,** 58–70.

Branicki, M., and S. Wiggins, 2010: Finite-time Lagrangian transport analysis: Stable and unstable manifolds of hyperbolic trajectories and finite-time Lyapunov exponents. *Nonlinear Processes Geophys.,* **17,** 1–36.

Brown, M. G., and K. B. Smith, 1991: Ocean stirring and chaotic low-order dynamics. *Phys. Fluids,* **3A,** 1186–1192.

Capet, X., J. C. McWilliams, M. J. Molemaker, and A. F. Shchepetkin, 2008: Mesoscale to submesoscale transition in the California Current system. Part I: Flow structure, eddy flux, and observational tests. *J. Phys. Oceanogr.,* **38,** 29–43.

Chelton, D. B., M. G. Schlax, R. M. Samelson, and R. A. de Szoeke, 2007: Global observations of large oceanic eddies. *Geophys. Res. Lett.,* **34,** L15606, doi:10.1029/2007GL030812.

d'Ovidio, F., J. Isern-Fontanet, C. López, E. Hernández-García, and E. Garcí-Ladona, 2008: Comparison between Eulerian diagnostics and finite-size Lyapunov exponents computed from altimetry in the Algerian basin. *Deep-Sea Res. I,* **56,** 15–31.

Ducet, N., P. Y. Le Traon, and G. Reverdin, 2000: Global high-resolution mapping of ocean circulation from TOPEX/Poseidon and *ERS-1* and *-2*. *J. Geophys. Res.,* **105,** 19 477–19 498.

Errico, R. M., 1985: Spectra computed from a limited area grid. *Mon. Wea. Rev.,* **113,** 1554–1562.

Franco, E., D. N. Pekarek, J. Peng, and J. O. Dabiri, 2007: Geometry of unsteady fluid transport during fluid-structure interactions. *J. Fluid Mech.,* **589,** 125–145.

Goni, G., and W. Johns, 2001: Census of warm rings and eddies in the North Brazil Current retroflection region from 1992 through 1998 using TOPEX/Poseidon altimeter data. *Geophys. Res. Lett.,* **28,** 1–4.

Green, M. A., C. W. Rowley, and G. Haller, 2007: Detection of Lagrangian coherent structures in three-dimensional turbulence. *J. Fluid Mech.,* **572,** 111–120.

Haller, G., 2001a: Distinguished material surfaces and coherent structures in 3D fluid flows. *Physica D,* **149,** 248–277.

——, 2001b: Lagrangian structures and the rate of strain in a partition of two-dimensional turbulence. *Phys. Fluids,* **13,** 3365–3385.

——, 2002: Lagrangian coherent structures from approximate velocity data. *Phys. Fluids,* **14,** 1851–1861.

——, and G. Yuan, 2000: Lagrangian coherent structures and mixing in two-dimensional turbulence. *Physica D,* **147,** 352–370.

Isern-Fontanet, J., B. Chapron, G. Lapeyre, and P. Klein, 2006: Potential use of microwave sea surface temperatures for the estimation of ocean currents. *Geophys. Res. Lett.,* **33,** L24608, doi:10.1029/2006GL027801.

Joseph, B., and B. Legras, 2002: Relation between kinematic boundaries, stirring, and barriers for the Antarctic polar vortex. *J. Atmos. Sci.,* **59,** 1198–1212.

Klein, P., and G. Lapeyre, 2009: The oceanic vertical pump induced by mesoscale eddies. *Ann. Rev. Mar. Sci.,* **1,** 351–375.

Kraichnan, R. H., 1971: Inertial-range transfer in two- and three-dimensional turbulence. *J. Fluid Mech.,* **47,** 525–535.

Lekien, F., and C. Coulliette, 2007: Chaotic stirring in quasi-turbulent flows. *Phil. Trans. Roy. Soc.,* **365A,** 3061–3084.

——, and J. Marsden, 2005: Tricubic interpolation in three dimensions. *Int. J. Numer. Methods Eng.,* **63,** 455–471.

——, and S. D. Ross, 2010: The computation of finite-time Lyapunov exponents on unstructured meshes and for non-Euclidean manifolds. *Chaos,* **20,** 017505, doi:10.1063/1.3278516.

——, S. C. Shadden, and J. E. Marsden, 2007: Lagrangian coherent structures in *n*-dimensional systems. *J. Math. Phys.,* **48,** 065404, doi:10.1063/1.2740025.

Le Traon, P.-Y., F. Nadal, and N. Ducet, 1998: An improved mapping method of multisatellite altimeter data. *J. Atmos. Oceanic Technol.,* **15,** 522–534.

——, Y. Faugére, F. Hernandez, J. Dorandeu, F. Mertz, and B. Ablain, 2003: Can we merge GEOSAT Follow-On with TOPEX/Poseidon and *ERS-2* for an improved description of the ocean circulation? *J. Atmos. Oceanic Technol.,* **20,** 889–895.

——, P. Klein, B. L. Hua, and G. Dibarboure, 2008: Do altimeter wavenumber spectra agree with interior or surface quasi-geostrophic theory? *J. Phys. Oceanogr.,* **38,** 1137–1142.

Liu, M., E. J. Muzzio, and R. L. Peskin, 1994: Quantification of mixing in aperiodic chaotic flows. *Chaos Solitons Fractals,* **4,** 869–893.

Mahadevan, A., and A. Tandon, 2006: An analysis of mechanisms for submesoscale vertical motion at ocean fronts. *Ocean Modell.,* **14,** 241–256.

Mancho, A. M., D. Small, and S. Wiggins, 2006: A comparison of methods for interpolating chaotic flows from discrete velocity data. *Comput. Fluids,* **35,** 416–428.

Mathur, M., G. Haller, T. Peacock, J. E. Ruppert-Felsot, and H. L. Swinney, 2007: Uncovering the Lagrangian skeleton of turbulence. *Phys. Rev. Lett.,* **98,** doi:10.1103/PhysRevLett.98.144502.

Obhukov, A. M., 1949: Structure of the temperature field in turbulent flows. *Izv. Akad. Nauk SSSR, Ser. Geofiz.,* **13,** 58–69.

Olascoaga, M. J., I. I. Rypina, M. G. Brown, F. J. Beron-Vera, H. Koçak, L. E. Brand, G. R. Halliwell, and L. K. Shay, 2006: Persistent transport barrier on the west Florida shelf. *Geophys. Res. Lett.,* **33,** L22603, doi:10.1029/2006GL027800.

——, F. J. Beron-Vera, L. E. Brand, and H. Koçak, 2008: Tracing the early development of harmful algal blooms on the west Florida shelf with the aid of Lagrangian coherent structures. *J. Geophys. Res.,* **113,** C12014, doi:10.1029/2007JC004533.

Padberg, K., T. Hauff, F. Jenko, and O. Junge, 2007: Lagrangian coherent structures and transport in turbulent magnetized plasmas. *N. J. Phys.,* **9,** doi:10.1088/1367-2630/9/11/400.

Pascual, A., Y. Faugère, G. Larnicol, and P.-Y. Le Traon, 2006: Improved description of the ocean mesoscale variability by combining four satellite altimeters. *Geophys. Res. Lett.,* **33,** L02611, doi:10.1029/2005GL024633.

Peacock, T., and J. Dabiri, 2010: Introduction to focus issue: Lagrangian coherent structures. *Chaos,* **20,** doi:10.1063/1.3278173.

Reniers, A. J. H. M., J. H. MacMahan, F. J. Beron-Vera, and M. J. Olascoaga, 2010: Rip-current pulses tied to Lagrangian coherent structures. *Geophys. Res. Lett.,* **37,** L05605, doi:10.1029/2009GL041443.

Rio, M.-H., and F. Hernandez, 2004: A mean dynamic topography computed over the World Ocean from altimetry, in-situ measurements and a geoid model. *J. Geophys. Res.,* **109,** C12032, doi:10.1029/2003JC002226.

Rossi, V., C. Lopez, E. Hernandez-Garcia, J. Sudre, V. Garcon, and Y. Morel, 2009: Surface mixing and biological activity in the four eastern boundary upwelling systems. *Nonlinear Processes Geophys,* **16,** 557–568.

Rypina, I. I., M. G. Brown, and H. Koçak, 2009: Transport in an idealized three-gyre system with application to the Adriatic Sea. *J. Phys. Oceanogr.,* **39,** 675.

Salman, H., J. S. Hesthaven, T. Warburton, and G. Haller, 2007: Predicting transport by Lagrangian coherent structures with a high-order method. *Theor. Comput. Fluid Dyn.,* **21,** 39–58.

Shadden, S. C., F. Lekien, and J. E. Marsden, 2005: Definition and properties of Lagrangian coherent structures from finite-time Lyapunov exponents in two-dimensional aperiodic flows. *Physica D,* **212,** 271–304.

——, J. O. Dabiri, and J. E. Marsden, 2006: Lagrangian analysis of fluid transport in empirical vortex ring flows. *Phys. Fluids,* **18,** 047105, doi:10.1063/1.2189885.

——, F. Lekien, J. D. Paduan, F. P. Chavez, and J. E. Marsden, 2009: The correlation between surface drifters and coherent structures based on high-frequency radar data in Monterey Bay. *Deep-Sea Res. II,* **56,** 161–172.

Shepherd, T. G., J. N. Koshyk, and K. Ngan, 2000: On the nature of large-scale mixing in the stratosphere and mesosphere. *J. Geophys. Res.,* **105,** 12 433–12 466.

Shuckburgh, E., H. Jones, J. Marshall, and C. Hill, 2009: Robustness of effective diffusivity diagnostic in oceanic flows. *J. Phys. Oceanogr.,* **39,** 1993–2009.

Stammer, D., 1997: Global characteristics of ocean variability estimated from regional TOPEX/Poseidon altimeter measurements. *J. Phys. Oceanogr.,* **27,** 1743–1769.

Stewart, R. H., C. K. Shum, B. Tapley, and L. Li, 1996: Statistics of geostrophic turbulence in the Southern Ocean from satellite altimetry and numerical models. *Physica D,* **98,** 599–613.

Swanson, K. L., and R. T. Pierrehumbert, 1997: Lower-tropospheric heat transport in the Pacific storm track. *J. Atmos. Sci.,* **54,** 1533–1543.

Tomsovic, S., and A. Lakshminarayan, 2007: Fluctuations of finite-time stability exponents in the standard map and the detection of small islands. *Phys. Rev.,* **76,** doi:10.1103/PhysRevE.76.036207.

Waugh, D. W., and E. R. Abraham, 2008: Stirring in the global surface ocean. *Geophys. Res. Lett.,* **35,** L20605, doi:10.1029/2008GL035526.

——, ——, and M. M. Bowen, 2006: Spatial variations of stirring in the surface ocean: A case study of the Tasman Sea. *J. Phys. Oceanogr.,* **36,** 526–542.

Witter, D. L., and A. L. Gordon, 1999: Interannual variability of the South Atlantic circulation from 4 years of TOPEX/Poseidon satellite altimeter observations. *J. Geophys. Res.,* **104,** 20 927–20 948.